Embedded, micro-interdigitated flow fields in high areal-loading intercalation electrodes towards seawater desalination and beyond

Vu Q. Do,[a] Erik R. Reale,[a] Irwin Loud IV,[a] Paul G. Rozzi,[a] Haosen Tan,[b] David A. Willis,[b] and Kyle C. Smith[a,c,d,e,*]

a. Department of Mechanical Science and Engineering, University of Illinois at Urbana-Champaign, Urbana, IL, USA

b. Department of Mechanical Engineering, Southern Methodist University, Dallas, TX, 75275

c. Department of Materials Science and Engineering, University of Illinois at Urbana-Champaign, Urbana, IL, USA

d. Computational Science and Engineering Program, University of Illinois at Urbana-Champaign, Urbana, IL, USA

e. Beckman Institute for Advanced Science and Technology, University of Illinois at Urbana-Champaign, Urbana, IL, USA

*corresponding author: kcsmith@illinois.edu

Abstract

Faradaic deionization (FDI) is a promising technology for energy-efficient water desalination using porous electrodes containing redox-active materials. Herein, we demonstrate for the first time the capability of a symmetric FDI flow cell to produce freshwater (<17.1mM NaCl) from concentrated brackish water (118mM), to produce effluent near freshwater salinity (19.1 mM) from influent with seawater-level salinity (496 mM), and to reduce the salinity of hypersaline brine from 781 mM to 227 mM. These remarkable salt-removal levels were enabled by using flow-through electrodes with high areal-loading of nickel hexacyanoferrate (NiHCF) Prussian Blue analogue intercalation material. The pumping energy consumption due to flow-through electrodes was mitigated by embedding an interdigitated array of <100 μm wide channels in the electrodes using laser micromachining. The micron-scale dimensions of the resulting embedded, micro-interdigitated flow fields (eμ-IDFFs) facilitate flow-through electrodes with high apparent permeability while minimizing active-material loss. Our modeling shows that these eμ-IDFFs are more suitable for our intercalation electrodes because they have >100X lower permeability compared to common redox-flow battery electrodes, for which millimetric flow-channel widths were used exclusively in the past. Total desalination thermodynamic energy efficiency (TEE) was improved by more than ten-fold relative to unpatterned electrodes: 40.0% TEE for brackish water, 11.7% TEE for hypersaline brine, and 7.4% TEE for seawater-salinity feeds. Water transport between diluate and brine streams and charge efficiency losses resulting from (electro)chemical effects are implicated as limiting energy efficiency and water recovery, motivating their investigation for enhancing future FDI performance.

Broader Context

During the past decade, the field of electrochemical separations has experienced a surge of research activity stimulated by the introduction of redox-active electrode materials, as motivated by their potential to increase salt removal, energy efficiency, and selectivity toward applications that support global sustainability, including desalination, CO_2 capture, environmental remediation, and nutrient/resource recovery. However, past experimental desalination studies with substantial salt removal have been limited to brackish water feeds when flow cells were used, despite our early modeling [Smith and Dmello, *J. Electrochem. Soc.*, **163**, A530 (2016)] that predicted seawater desalination using cells comprised of symmetric cation intercalation electrodes, separated by cation-blocking membranes. This work is the first to demonstrate experimental salt removal approaching seawater salinity by using high areal-loading flow-through intercalation electrodes that are engraved with interdigitated microchannel networks to minimize electrical and pumping energy consumption. This new paradigm for the structuring of porous electrodes motivates the further development of embedded microfluidic networks and their use in various electrochemical processes with liquid or gaseous feeds, including flow batteries for energy storage, fuel cells for energy conversion, and electrochemical CO_2 conversion.

Introduction

With the global human population growing at an ever increasing rate and demanding more water for domestic, agricultural, and industrial purposes, desalination of brackish water and seawater is considered an alternative to freshwater resources and is expected to produce more than 200 million m^3 per day in 2030.[1] Reverse osmosis (RO) presently contributes nearly 70% of global desalination capacity, followed by thermal-based processes with ~25%.[2,3] However, thermal distillation is energy intensive[4] due to the heat of vaporization of water. While RO is energy efficient,[5] its water recovery is mechanically limited by the pressure necessary to overcome osmosis into highly concentrated saltwater.[6] Further, both such processes result in the indiscriminate removal of salt, thus requiring remineralization.[7,8] In addition, RO plants require large capital investment, substantial maintenance, and present environmental impacts caused by pretreatment chemicals and membrane cleaning.[9]

Desalination that uses electric fields to transport ions, rather than using pressure to transport water molecules as in RO, promises reduced brine volume and environmental impact. Hybrid RO systems that employ electrodialysis to increase water recovery have been analyzed[10,11] and demonstrated,[12,13] but electroosmosis through electrodialysis stacks was shown to limit the degree of brine concentration.[10] Further, the use of gas-evolution electrodes in electrodialysis stacks with only a few membrane pairs results in large energy consumption due to the large difference in electrode potentials (~1 V when using H_2 and O_2 evolution). Alternatively, capacitive deionization (CDI) using ion adsorption in electric double layers (EDLs) has achieved better energy efficiency than RO at brackish salt concentrations (<10 g L^{-1} or 171mM NaCl)[14] with

much research focused on developing high-capacity, high-rate electrode materials.[15,16] Even with advanced materials, salt adsorption capacity (SAC) using EDLs rarely exceeds 15 mg per gram of active material,[17] and thermodynamic energy efficiency (TEE) remains below 10%.[18,19] This is after modifications to CDI process design that have yielded greater improvements in SAC and TEE, demonstrating the importance of system optimization.[18] For example, using ion-exchange membranes in CDI can improve TEE by one order of magnitude,[19] and flow-electrode CDI can improve SAC by >50%.[20,21] Despite these advances, CDI using EDL charge storage has been relegated to brackish water desalination, mainly due to its low capacity.

In contrast, redox-active intercalation materials used in Faradaic deionization (FDI) promise seawater desalination on the basis of experiments with non-flowing cells[22,23] and earlier modeling with flowing cells.[24,25] This can be attributed to their high ion-storage concentrations (>4 mol L^{-1} in Ref. 26) and large SACs (as large as ~100 mg g^{-1} in Ref. 27). Despite this, the desalination of seawater salinity in a practical FDI flow cell using intercalation electrodes remains to be demonstrated experimentally. Past FDI studies[23,26,28–33] have used porous electrodes incorporating Prussian blue analogue (PBA) intercalation material at PBA mass loadings under 10 mg cm^{-2} to remove less than 20% of the salt from feeds with seawater salinity. However, the salt removal from these studies shows a positive correlation between electrode capacity and salt removal (Fig. 1a). This observation suggests scaling up charge capacity as a means to approach seawater desalination, as we demonstrate subsequently by upsizing electrodes.

Aspects of device architecture other than capacity have significant impacts on SAC, salt adsorption rate (SAR), and TEE.[19,34] Among existing flow-cell configurations,

symmetric FDI cells[24,25,35] have outperformed hybrid CDI, dual-ion desalination, and the desalination battery.[19,34] In addition, flow-through electrodes[25,26,28,30,36] have been shown to outperform flow-by electrodes.[25,30,36] The enhanced performance of flow-through electrodes is a result of the intimate contact of flowing salt solution with intercalation material that enables salt-depleted solution within electrodes to be evacuated and replaced efficiently with new salt-rich solution (see SI and Fig. S1). Therefore, flow-through configurations remove salt faster while yielding higher utilization of active material capacity. However, the fine porosity of electrodes containing intercalation nanoparticles (e.g., PBAs) produces large pumping losses in flow-through configuration because (1) pumping energy E_{pump} scales with the square of pressure drop Δp for a desired volumetric flow rate Q under creeping-flow conditions ($E_{pump} \propto Q\Delta p \propto \Delta p^2$)[28] and (2) Δp scales inversely with electrode hydraulic permeability k_h that scales with the square of pore size. While past FDI studies have neglected pumping losses,[37] we have shown recently that pumping losses can exceed electrical energy input by 50-fold in flow-through FDI.[26] Large-area electrodes also result in increased pumping pressure due to increased flow path length, further suppressing desalination energy efficiency and further necessitating a means of its mitigation to make flow-through FDI viable.

In this work, we report symmetric FDI with flow-through nickel hexacyanoferrate (NiHCF) electrodes approaching the removal of seawater salinity levels, while achieving pumping losses at parity with or lower than electrical losses for the first time (Fig. 1c). These salt removal levels were achieved with high areal-loading electrodes having NiHCF loadings greater than 19 mg cm^{-2}, together with an automated valve-switching

system to recirculate feed water so as to minimize state-of-charge gradients caused by streamwise polarization induced by salt concentration gradients.[26,36] Pumping losses were reduced by more than ten-fold by increasing hydraulic permeation through intercalation electrodes by embedding interdigitated microchannels within them via laser micromachining, resulting in novel embedded, micro-interdigitated flow fields (eμ-IDFFs). Past CDI studies using through-plane flow-through electrodes have avoided excessive pumping energy by using electrode materials with large macropores[38] and laser-perforated macrochannels.[39] However, such approaches are incompatible with FDI where an impermeable membrane is used to separate electrodes,[26,28,30] thus requiring in-plane fluid distribution.

For in-plane distribution of fluid through electrodes in redox-flow batteries[40,41] (RFBs) and fuel cells, various flow fields including interdigitated ones (IDFFs) have been used.[42] With one exception,[40] the past use of in-plane flow fields has embedded them in ~1 cm thick bipolar plates that compress monolithic carbon electrodes, whereas we presently embed them within intercalation electrodes that are cast on a ~100 μm graphite foil, thus yielding a low-profile design that minimizes the cost and mass of inactive cell components. Further, the apparent hydraulic permeability k_h^{app} produced by embedding IDFF channels of width w scales as $k_h^{app} \sim w^{-2}$ (see SI) when fixing the ratio of channel width to inter-channel spacing s, motivating IDFF miniaturization presently. Despite this, Fig. 1b shows that channel widths and inter-channel spacings of past IDFFs and other flow fields used for RFBs are ten-fold larger than the present eμ-IDFFs that we introduce and demonstrate for the first time. The eμ-IDFFs introduced here are shown to produce transverse flow between interdigitated microchannels less

than 100 μm wide with as much as 100-fold enhanced permeability when embedded in intercalation electrodes, despite producing parallel flow and less than four-fold enhanced permeability when embedded in carbon-felt electrodes used in RFBs.

In what follows we first introduce rational design criteria for eμ-IDFFs using physics-based modeling of flow-through porous electrodes patterned with macro- and micro-porosity, identifying a key dimensionless parameter that justifies the use of microchannels despite the exclusive use of millimetric channels in earlier IDFFs for RFBs. Subsequently, the results of eμ-IDFF fabrication by laser micromachining are presented, where the imbibing of electrodes with water before laser micromachining is shown to minimize heat affected zones and improve channel quality. Next, we report results of desalination experiments using a symmetric FDI cell using eμ-IDFFs with feed-water recirculation. The pair of electrodes having the highest loading achieved 93.5%, 96% and 70.9% salt removal from brackish water (118 mM NaCl), seawater-salinity (496 mM), and hypersaline (781 mM) feeds, respectively. Because pumping energy was reduced significantly using eμ-IDFFs, TEE approached 40% for brackish water desalination and ~10% for seawater and hypersaline brine desalination. Desalination experiments using unpatterned electrodes were also conducted, showing 23% lower specific capacity compared to that of patterned electrodes, indicating that eμ-IDFFs help to minimize dead volumes within dense electrodes. Water recovery in excess of 50% is reported with water transport and charge efficiency loss mechanisms identified as future means of enhancement of desalination performance.

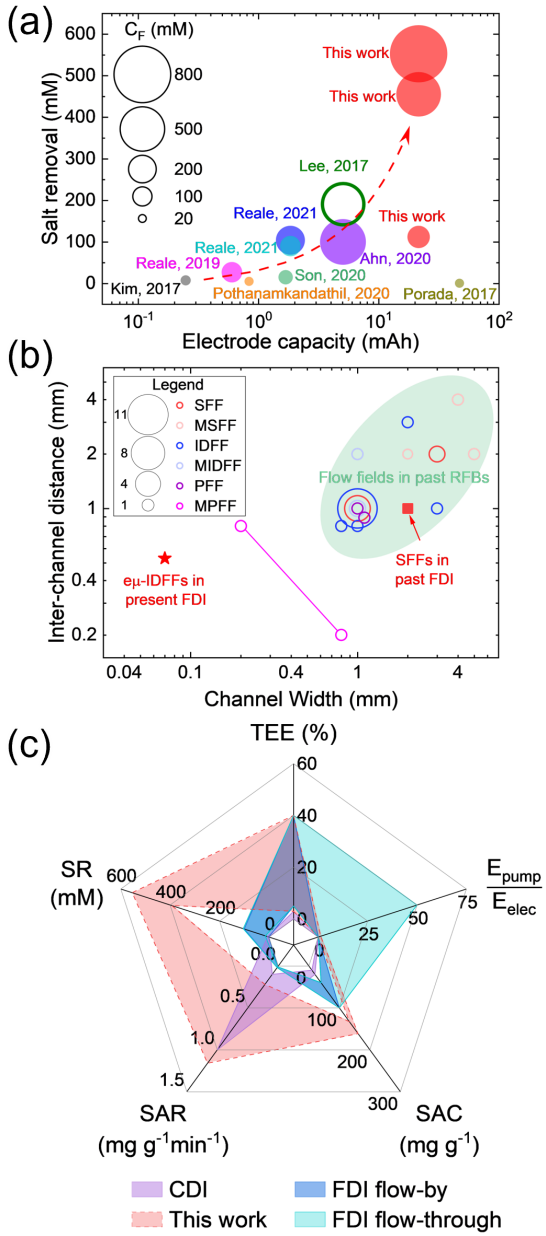

Figure 1. (a) Salt removal achieved presently compared to previous work using flow cells with NiHCF electrodes (Table S1). Area of a bubble is proportional to the feed concentration C_F used in the work it represented. (b) Inter-channel distance and channel width for interdigitated (IDFFs), serpentine (SFFs), and parallel (PFFs) flow fields and modified versions thereof (MFFs) used presently and used previously in RFBs[43,44,53–62,45,63–67,46–52] and FDI[68] (Table S2). The area of a given bubble is proportional to the number of flow fields using such dimensions. The dumbbell symbol is for a corrugated MPFF having channel sections of alternating width and spacing.[69] (c) Radar plot comparing desalination metrics of the present work with those of past FDI and CDI work (Table S3).[17,19,23,26,28–33]

Results and Discussion

Design and Fabrication of eμ-IDFFs

We fabricated three pairs of electrodes with different nickel hexacyanoferrate (NiHCF) loading levels to embed them with eμ-IDFFs and to subsequently characterize their desalination performance in a symmetric FDI flow cell. After drying, all electrodes were found to be crack free (Fig. 2b) with thicknesses between 400 and 450 μm, and each was subsequently calendered down to ~200 μm (excluding the graphite foil which is ~100 μm thick). Next, laser micromachining was used to engrave eμ-IDFFs into these electrodes using the design shown in Fig. 2d. Properties of the six electrodes from these three pairs are shown in Table 1, where L, M, and H denote electrode pairs with lowest (~15 mg cm^{-2}), medium (~19 mg cm^{-2}), and highest (~21 mg cm^{-2}) NiHCF loading.

Table 1. Properties of electrodes after calendaring. The apparent permeabilities k_h^{app} were measured after electrodes were engraved with eμ-IDFFs.

Pair ID	Electrode ID	NiHCF loading (mg cm^{-2})	Porosity, ε (%) (uncalendared)	Porosity, ε (%) (calendared)	Permeability, k_h^{pe} (μm^2)	Apparent permeability, k_h^{app} (μm^2)
L	1	15.3	64.3	46.5	0.69	121.46
	2	15.3	64.3	46.5	1.06	52.99
M	3	19	62.0	42.2	0.63	60.98
	4	18.6	60.0	43.5	0.236	36.4
H	5	21.5	57.0	39.8	0.58	31.04
	6	21.3	57.4	40.4	0.48	31

The eμ-IDFFs that we have embedded in intercalation electrodes increase apparent hydraulic permeability by 30- to 120-fold (Table 1) by reducing the flow path length through electrodes by ~100-fold from 4.5 cm down to 500 μm (Fig. 2a). As we subsequently show, the width of microchannels must be sufficiently large to achieve uniform flow through porous-electrode regions while also being sufficiently small to

minimize material loss due to the embedding of eμ-IDFFs. The former attribute is critical to ensure that salt-rich solution is supplied everywhere within the electrode to maximize intercalation-material utilization, whereas the latter is essential to maintain high charge capacity post-engraving.

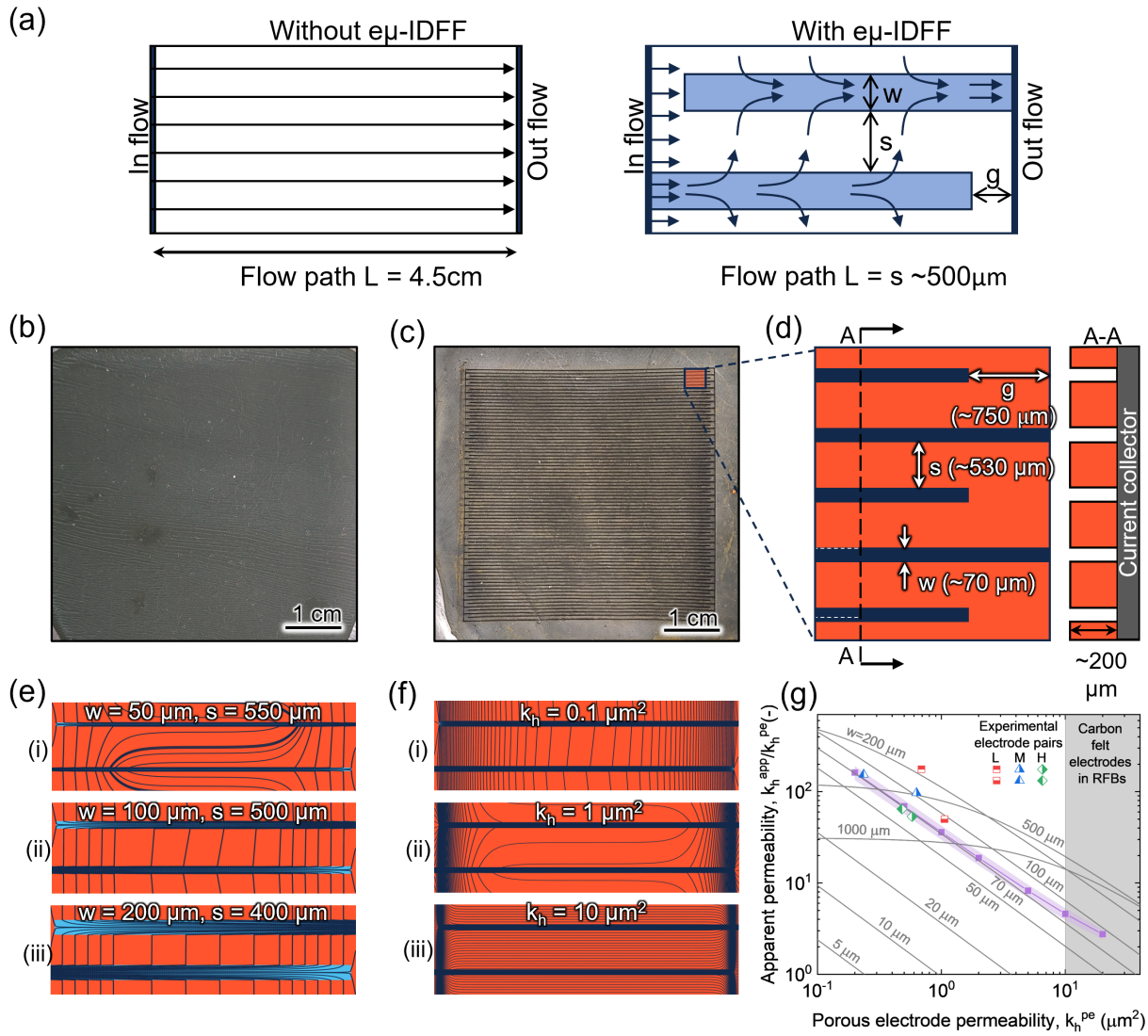

Figure 2. (a) Schematics comparing the flow path of electrodes with and without eμ-IDFFs. Photos of electrodes (b) after drying and (c) after being calendared and engraved with an eμ-IDFF. (d) Dimensions of the chosen eμ-IDFF design with a cross-section shown through the A-A plane. (e) Calculated streamlines for three cases with different channel width w and inter-channel distance s. The gap g and electrode permeability k_h^{pe} were kept constant at 750 μm and 0.28 μm^2. (f) Calculated streamlines for three cases with the same channel dimensions shown in (d) but with electrode permeability varying. (g) Predicted and experimental ratios between the apparent

permeability of each patterned electrode k_h^{app} to porous-electrode permeability k_h^{pe}. Purple symbols indicate data obtained from the numerical model using the channel dimensions shown in (d). Gray lines indicate data obtained using the quasi-1D analytical model for various channel widths with a fixed ratio of channel width to inter-channel distance equal to 70/530. The shaded region represents the typical range of permeability of carbon felt electrodes in RFBs.[70–72]

To rationalize these tradeoffs, we predicted the spatial variation of superficial velocity $\vec{u}_s$ by solving Darcy's law subject to volume conservation: $\vec{u}_s = -(k_h/\mu)\nabla p$ and $\nabla \cdot \vec{u}_s = 0$, where p and μ are pressure and dynamic viscosity, respectively. Here, hydraulic permeability k_h depends on the phase associated with a given position: (1) micro-porous intercalating regions use the hydraulic permeability of unpatterned porous electrode material k_h^{pe}, whereas (2) macro-porous eμ-IDFF regions use a hydraulic permeability k_h^{ch} that reproduces the axial-pressure/mean-velocity relationship resultant from Poiseuille flow through a given channel's cross-section. Our approach is an extension of Darcy-Darcy formulations that are routinely used to model flow through fractured, micro-porous rock.[73]

Channel width w, inter-channel distance s, and the gap between each channel's tip and the electrode's edge g were varied to study their effects on the uniformity of the streamlines produced by a given eμ-IDFF design. Assuming $k_h^{pe} \approx 0.3$ μm^2, streamlines approach a perpendicular orientation to channel surfaces (i.e., transverse flow) for microchannels wider than 50 μm. Further, the model predicts more uniform flow through the porous electrode region between two adjacent microchannels with increasing w and decreasing s (Fig. 2e). Also, g that is too large results in dead zones near channel tips, whereas g that is too small suppresses transverse flow through the porous electrode (see SI and Figs. S3, S4). To understand the impact of the

experimental variations of k_h^{pe} (see Table 1) with various k_h^{pe}, we simulated the streamlines of the eμ-IDFF design sought later experimentally (w = 70 μm, s = 530 μm, and g = 750 μm) that limits active material loss to approximately 11%. While low enough k_h^{pe} values produce transverse flow, flow parallel to channels results from increasing k_h^{pe} to values that are too large. The resulting apparent permeability values predicted among the different electrode samples agree well with experimental values as shown in Fig. 2g.

A simplified quasi-1D analytical model (see SI) also reveals that the transitions observed when varying channel width and when varying k_h^{pe} are captured by a critical value of a common dimensionless parameter $\Xi = k_h^{pe} L^2/(w^3 s)$ that represents the characteristic ratio of channel hydraulic resistance to porous-electrode hydraulic resistance. Designs with $\Xi < 1$ assure that streamlines are routed between channels within porous electrode regions, rather than parallel to them, because of the finite transverse velocity produced across a given channel's entire length (Fig. S6a). This criterion explains why microchannel eμ-IDFFs produce effective flow-through intercalation electrodes, though microchannel eμ-IDFFs produce parallel flow for the high-permeability electrodes used commonly in RFBs. To produce the same Ξ value, an RFB electrode with 10 μm^2 permeability must have three-fold larger channel width than an FDI electrode with 0.3 μm^2 permeability (assuming a common electrode length L and inter-channel distance s), since $w_{FDI}/w_{RFB} = \left(k_{h,FDI}^{pe}/k_{h,RFB}^{pe}\right)^{1/3}$ is satisfied for FDI and RFB designs subject to such conditions. Thus, the use of microchannel eμ-IDFFs is not a simple extension of the past use of IDFFs in RFBs, and their ability to facilitate transverse flow is enabled by the patently low permeability of the porous material in

286 which they are embedded. We also used the quasi-1D model to find a closed-form
287 expression for eμ-IDFF apparent permeability (see SI), which is in good agreement with
288 our numerical results using a channel width of 70 μm (Fig. 2g). By using the quasi-1D
289 model, Fig. 2g also shows that to produce a normalized apparent permeability
290 exceeding unity microchannels must exceed a certain critical width w_{cr} that decreases
291 with decreasing porous electrode permeability (Fig. S6c).

292 Understanding of laser/electrode interactions is critical to fabricate eμ-IDFFs that
293 approach felicitous designs and that maintain the integrity of the underlying electrode
294 material. We characterized the microstructure and composition of electrode material
295 and the morphology of microchannels by engraving separate microchannels at various
296 laser powers. At high laser power density we observed heat-affected zones (HAZs) that
297 extend away from channel edges. Within such regions electrode material shows a
298 permanent change in color from dark green to black (Fig. 3b) that is attributed to the
299 structural decomposition of NiHCF, as evidenced by the disappearance of the C≡N
300 peak at ~2160 cm^{-1} in local Raman spectra at channel walls (Fig. 3d). Such changes
301 suggest that the temperature at the laser-irradiated surface exceeds the onset of the
302 NiHCF decomposition event at 395^{o}C, as observed from thermogravimetric analysis
303 (Fig. 3e). Further, the coarsening of electrode material in HAZs is likely due to the
304 melting of PVDF at approximately 160^{o}C.[74]

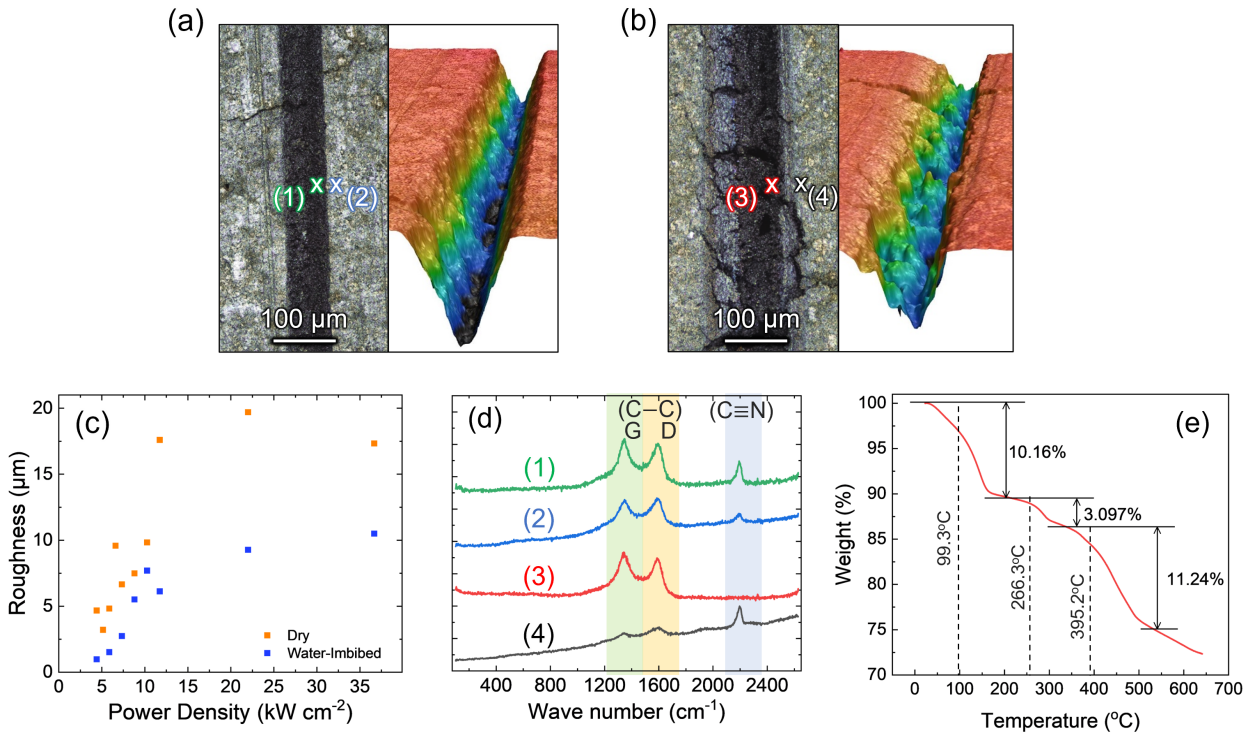

Figure 3. Optical and 3D profilometry images of microchannels engraved using (a) a water-imbibed electrode and (b) a dry electrode. (c) The root-mean-square (RMS) surface roughness of the channels made on dry and water-imbibed electrodes at different power densities. (d) Raman spectra measured inside and outside of channels made by water-imbibed engraving [(1) and (2) in (a)] and dry engraving [(3) and (4) in (b)]. Peaks at 1350 cm^{-1}, 1580 cm^{-1}, and 2300 cm^{-1} are signatures of the D- and G-bands of C-C vibration and of C≡N bonds. (e) Thermogravimetric analysis of a calendered electrode showing water evaporation below 300°C and the decomposition of NiHCF at 395°C.

To mitigate these effects, we also performed laser micromachining on electrodes imbibed with water, inspired by water-assisted laser micromachining of non-porous materials.[75,76] Not only did water-imbibed engraving minimize HAZs (Fig. 3a), it also created smoother channels that are evidenced by smaller root-mean-square surface roughness within channels (Figs. 3c). These effects result from the ability of water to absorb some of the heat and mitigate the temperature rise in the electrode material surrounding the irradiated region and to prevent PVDF coarsening at 160°C and NiHCF decomposition at 395°C. The smaller thermal diffusivity[77] α of liquid water (0.15 mm^2/s)

relative to air (20 mm^2/s) suggests ten-fold smaller penetration depth δ_P into HAZs when using water-imbibed engraving ($\delta_P \sim \sqrt{\alpha\tau}$ over time-scale τ), in addition to the potential for thermal protection of HAZs due to the enthalpy of water vaporization.† Using these results, we determined specific laser settings to achieve the desired eμ-IDFF dimensions while minimizing HAZs (see SI). While the targeted eμ-IDFF design had microchannels with a 70 μm wide by 200 μm deep rectangular cross-section (Fig. 2d), their fabrication proved challenging due to the laser beam's tendency to engrave side walls that deviate from vertical orientation (Figs. 3a,b), likely as a result of its Gaussian intensity distribution. Therefore, we engraved microchannels with similar cross-sectional area to the felicitous design (14,000 μm^2) to produce similar hydraulic resistance, the dimensional characterization of which is included in the SI.

Desalination Experiments using eμ-IDFFs

We performed desalination experiments using electrodes fabricated with eμ-IDFFs in a symmetric FDI flow cell (Fig. 4a and Fig. S13). During each desalination half-cycle one electrode captures cations to produce desalinated water while the other releases intercalated cations to produce brine. At the end of each half-cycle the former electrode approaches 100% state-of-charge (SOC) while the latter approaches 0% SOC. The applied current is then switched off and the FDI cell enters an open-circuit (OC) mode at t_1. To enable continuous desalination via the switching of electrical current we used a tubing system with four fluidic valves to switch inlet and outlet streams,[26] the effect of which is illustrated in Fig. 4b. A pause period ($\Delta t_{pause} = t_3 - t_2$)

†At the ~100 ns time-scale for laser irradiation, water evaporation occurs at higher temperatures and pressures than at equilibrium,[78] thus requiring further investigation to quantify the relative impacts of water's sensible and latent heating on HAZs during water-imbibed engraving.

is then used between the time instants at which inlet (t_2) and outlet (t_3) switching events occur to allow diluate and brine within the FDI cell to evacuate into their respective reservoirs. This pause period minimizes effluent intermixing but cannot eliminate it completely. Typical real-time variations of cell potential, current, and diluate concentration during a desalination experiment are shown in Fig. 4c. During a given half-cycle, cell potential increases to 0.4 V or decreases to -0.4 V depending on the direction of the applied current.

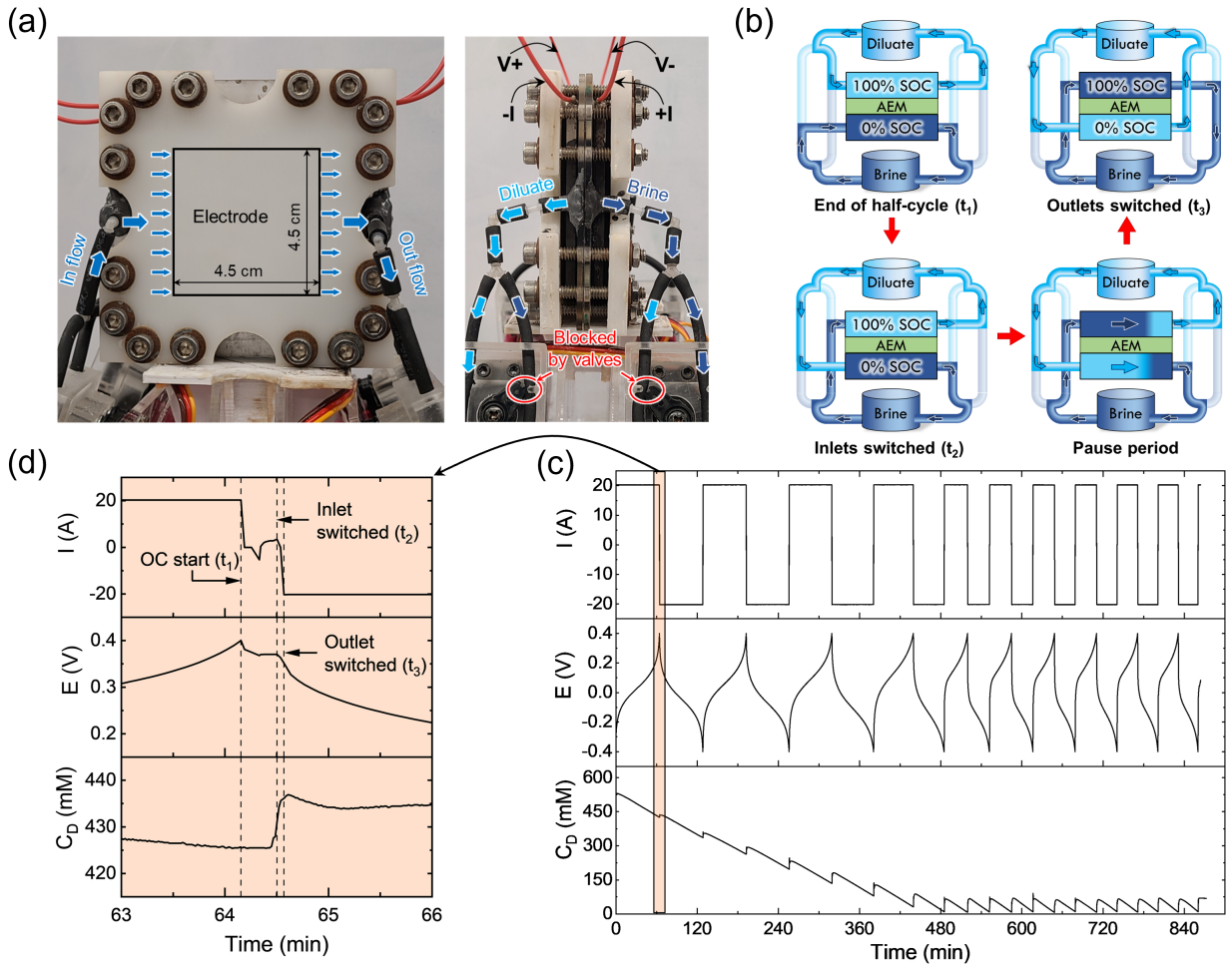

Figure 4. (a) Photos of the FDI flow cell with flow directions and applied current/voltage annotated, (b) schematic of the flow cell with fluid recirculation system during valve switching, with electrodes having disparate SOC. A half-cycle ends at t_1 and the applied current is terminated to produce open-circuit conditions, during which potential-controlled electrochemical impedance spectroscopy is performed. At t_2 the two inlet valves are switched. A pausing time Δt_{pause} is used to let diluate and brine within the

FDI cell evacuate into the correct reservoir. After Δt_{pause} the outlet valves are switched at t_3. A similar sequence is used to switch the system back to its original state (i.e., the state at t_1) after cycling with oppositely signed current. (c) Time variation of FDI cell potential, applied current, and diluate-reservoir concentration from a desalination experiment using H-pair electrodes (21 mg cm^{-2}) with 1 mA cm^{-2} applied current density. The shaded region is zoomed in and shown in (d).

The salt concentration in the diluate reservoir decreases continuously during each half-cycle (Fig. 4c) and rapidly increases for a short period of time after valve switching at the end of each half-cycle (Fig. 4d) due to effluent intermixing.[26] As a result such jumps in diluate-reservoir concentration become more pronounced as the difference in salt concentration between reservoirs becomes larger. The salt-concentration increase that results from such mixing eventually becomes large enough to match the salt removal obtained due to the applied current, thus limiting overall salt removal of the multi-cycle desalination process.

For feed water having salt concentration C_F near seawater salinity, desalination experiments were conducted at 5 mL min^{-1} flow rate with 1 mA cm^{-2} current density. As shown in Fig. 5a, salt removal increases with increasing NiHCF loading from nearly 90% for L-pair electrodes (15 mg cm^{-2}) to 95% for M-pair electrodes (19 mg m^{-2}) to 96% for H-pair electrodes (21 mg cm^{-2}). Diluate feed concentration also decreased from 496 mM NaCl respectively to 102 mM, 23.7 mM, and 19.1 mM as a result of desalination using these electrode pairs. These results confirm our hypothesis that scaled-up FDI cells with high-capacity electrodes increase salt removal: increasing NiHCF loading by 40% from 15 mg cm^{-2} to 21 mg cm^{-2} reduced effluent concentration from brackish water salinity (102 mM) to near-potable salinity (19.1 mM), which is also the lowest salinity produced from such high-salinity feeds using CDI or FDI to our knowledge.

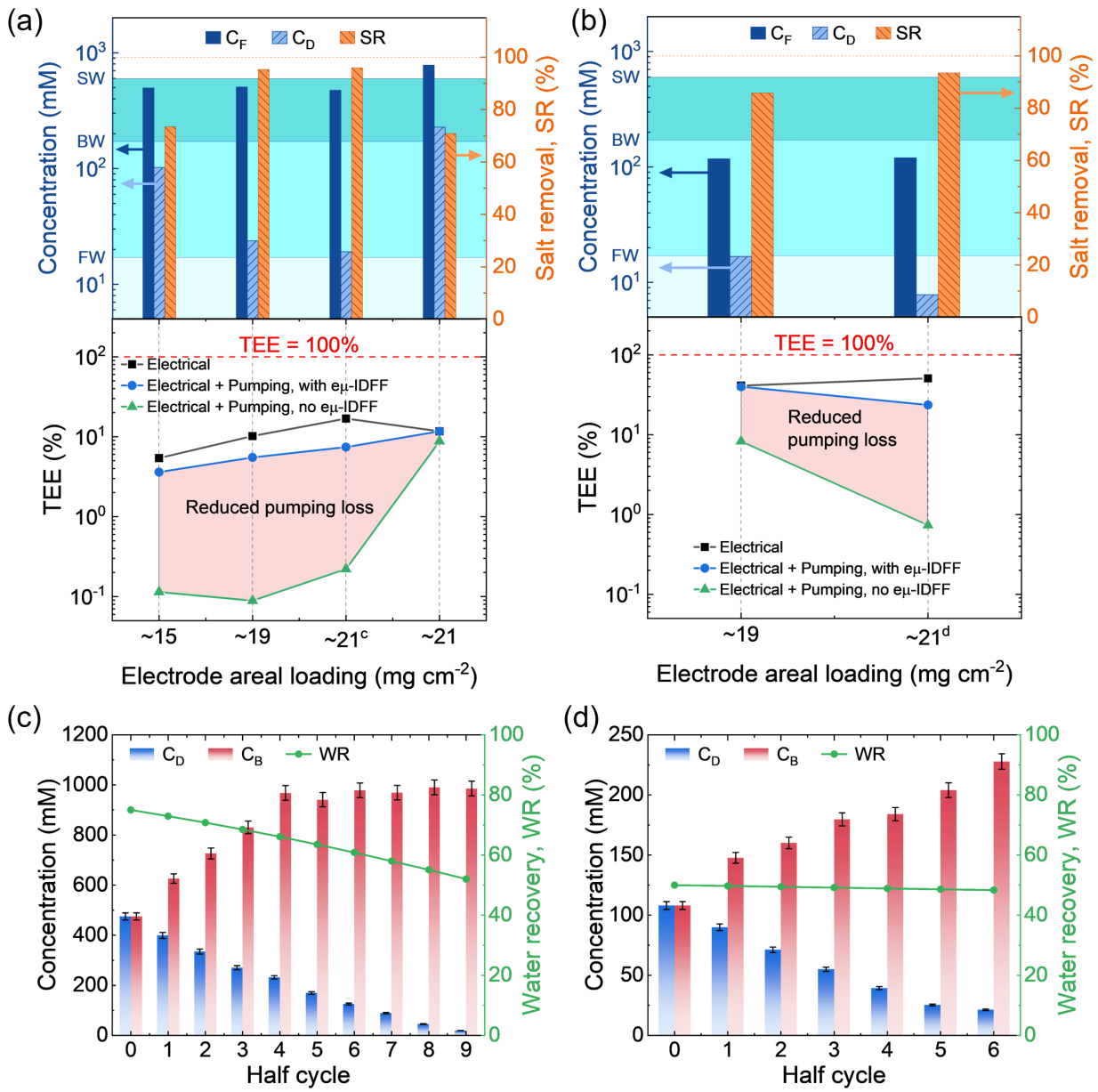

Figure 5. (a) Desalination of feed water with near seawater level salinity (SW, ~35 g L^{-1} or 599 mM NaCl) down to brackish water level salinity (BW, <10 g L^{-1} or 171 mM NaCl) and freshwater level salinity (FW, ~1 g L^{-1} or 17 mM NaCl) and their corresponding thermodynamic energy efficiencies (TEEs). (b) Desalination of brackish water down to freshwater level salinity using different electrode loading levels and the resulting TEEs. The cycle dependence of diluate and brine reservoir concentrations for brackish and seawater experiments are shown in (c) and (d), respectively. The following symbols are used throughout: C_F for feed concentration, C_D for diluate concentration, C_B for brine concentration, SR for salt removal, and WR for water recovery. Cyclic-specific data for all six experiments is provided in the SI (Fig. S14, S15).

Figures 5a,b show the corresponding thermodynamic energy efficiency (TEE) of these experiments considering (i) measured electrical input alone, (ii) measured electrical input and pumping energy calculated using the measured apparent permeability (with eμ-IDFF), and (iii) electrical input and pumping energy calculated using porous-electrode permeability (no eμ-IDFF). Using such dense and highly loaded electrodes without eμ-IDFFs is accompanied by infeasibly large pumping energy that decreases overall TEE. When considering only electrical energy input, the respective TEEs for L-, M-, and H-pair electrodes were 5.4%, 10.2%, and 17.0%. However, these respective TEEs diminished dramatically to 0.11%, 0.09%, and 0.22% when taking into account pumping energy without eμ-IDFFs. By engraving eμ-IDFFs into these electrodes, TEE was improved to 3.6%, 5.5%, and 7.4% due to 30- to 120-fold increases in their apparent permeabilities. These TEEs are at parity with past FDI experiments using intercalation materials, despite feed water salinity in such work being limited to 25 mM or less.[19] The pumping-energy saved by using eμ-IDFFs (shaded regions in Fig. 5a) indicates the essential role that eμ-IDFFs provide in enhancing FDI TEE using flow-through electrodes.

We also carried out desalination experiments on hypersaline brine using 21 mg cm^{-2} H-pair electrodes. These experiments were able to use decreased flow rate (1 mL min^{-1}) and increased current density (8.5 mA cm^{-2}), owing to the decreased SOC gradients and ohmic resistance expected for such brines. We observed a diluate concentration decrease of 71% from 781 mM initially to 227 mM as a result (Fig. 5a), demonstrating for the first time the potential of FDI using cation intercalation electrodes to treat concentrated brines. Furthermore, this level of salt removal was achieved with

11.7% TEE irrespective of whether pumping energy was included or not. The insignificance of pumping energy in this context can be understood in the following manner. E_{pump} is the product of hydraulic resistance R_h, the square of volumetric flowrate Q, and desalination batch time Δt: $E_{pump} = R_h Q^2 \Delta t$, where R_h is proportional to overall electrode length L and is inversely proportional to the apparent hydraulic permeability k_h^{app} according to Darcy's law ($R_h = \mu L/(k_h^{app} A)$, where A is the area of the electrode's inlet plane). Therefore, pumping energy at higher current density decreases as desalination batch time shortens, and consequently its contribution to TEE losses becomes less significant in that limit. This finding suggests that using electrodes tailored to operate at high current density and low flow rate could further decrease pumping energy and improve overall TEE.

For brackish water desalination, the use of eμ-IDFFs results in exceptional TEE. Two experiments were conducted in which M-pair (19 mg cm^{-2}) and H-pair (21 mg cm^{-2}) electrodes were used to desalinate feed water with ~100 mM NaCl at 1 mA cm^{-2}. As shown in Fig. 5b, salt concentration decreased from 118mM to 16.7 mM for M-pair and to 7.8 mM for H-pair, both of which are below the salinity of fresh water (17 mM). With eμ-IDFFs the TEE for M-pair electrodes increased from 8.3% to 40.0% and that of H-pair electrodes increased from 0.7% to 23.6%. The higher TEE of the former case is due to the use of a smaller flowrate (1 mL min^{-1} compared to 5 mL min^{-1} in the latter case). These TEEs approach that of a single stage RO system without energy recovery, according to recent analysis.[79]

We also find that eμ-IDFFs increase TEE not only by improving electrode hydraulic permeability but also by maximizing active-material capacity utilization. Figure

443 S16 shows the specific capacity versus cycle number obtained from desalination
444 experiments using the L-, M-, and H-pair electrodes with eμ-IDFFs, along with that of an
445 unpatterned electrode pair. In all cases a seawater-salinity feed was used. The
446 electrodes with eμ-IDFFs consistently show specific capacities greater than 55 mAh g^{-1},
447 whereas the unpatterned electrodes show a maximum specific capacity of 47 mAh g^{-1}
448 only for the first half-cycle and subsequently show steadily decreasing capacity. This
449 effect may be a result of dead volume within porous electrodes that is formed during
450 calendering, where an initially interconnected porous network (~60% porosity) is
451 compressed into a dense microstructure having approximately 40% porosity. As the
452 porous network collapses, the solid constituents fill micropores to form isolated pockets
453 to which fluid delivery is impeded during desalination experiments, potentially causing
454 insufficient salt delivery to intercalation material and thus reducing capacity. Engraving
455 electrodes with eμ-IDFFs likely opens such isolated pores to enable intercalation
456 material to access fresh salt solution.

457 Water recovery (WR), defined as desalinated water volume divided by total feed-
458 water volume, was determined at the end of each desalination half-cycle. While
459 terminal WR exceeded 50% for all experiments (Figs. 5c,d), seawater and hypersaline
460 brine feeds showed gradually decreasing WR with increasing salt removal (Fig. 5c),
461 thus requiring compensation by using increased initial diluate volume to achieve 50%
462 terminal WR. From this data we determined water transport rates between diluate and
463 brine as high as 0.16 L m^{-2} h^{-1} (Table S5). Following past theoretical analysis for
464 osmosis/electroosmosis through ion-exchange membranes (IEMs),[80–82] we predict a
465 maximum water transport rate through Neosepta AMX as 0.20 and 0.25 L m^{-2} h^{-1} when

using respective salt concentrations of 496 mM and 781 mM and assuming 40 vol.% water therein. These values are consistent with previous measurements on commercially available membranes,[83] ED stacks,[84] and RFBs[85] (0.24 – 2.46 L m^{-2} h^{-1}), making water flux through IEMs a probable mechanism of WR loss among other factors.

Despite the promising TEEs achieved in comparison with prior CDI and FDI literature, our results indicate significant room for improvement relative to the thermodynamic limit of energy consumption, especially for high-salinity feeds. For this reason we analyzed process charge efficiency[86] (CE), defined as the ratio of cationic charge desalinated to electrical charge transferred. In general, CE was shown to decrease with increasing feedwater salinity. Despite brackish feeds with less than 100 mM NaCl exhibiting nearly ideal CE (Fig. S15), we observed a decrease of CE to ~50% when using seawater salinity feeds (Fig. S14). To isolate CE losses due to effluent intermixing (a type of 'flow efficiency' loss mechanism[87,88]) we performed separate desalination experiments for a single half-cycle (i.e., experiments without valve or current switching) that used H-pair electrodes (21 mg cm^{-2}) with various feed concentrations. These experiments showed CE dropping linearly from 91.7% to around 50% as feed concentration increased from 38 mM to more than 500 mM (Fig. S17a). Since our electrodes exhibited excellent cyclability with no decrease in specific capacity after 90 cycles (Fig. S17b), this concentration-dependent CE likely results from mechanisms other than electrode degradation, such as gas-evolution/-consumption reactions or the loss of membrane permselectivity. Further, Fig. 2f shows that, even though the chosen eμ-IDFF generates streamlines that are perpendicular to microchannels, streamlines are concentrated near electrodes edges, exhibiting a

degree of non-uniformity in fluid distribution. In addition, dead zones could exist within the electrode microstructure as a result of its heterogeneous nature, and side reactions occurring because of salt depletion within dead zones would lead to lower CE. On the other hand, selectivity losses are ubiquitous in membrane processes such as electrodialysis and ion concentration polarization.[89] When the counter-ion concentration around an IEM exceeds the concentration of the fixed-charge groups within the IEM, co-ions can penetrate into the IEM to cause co-ion leakage that acts against deionization.[89,90] Hence, IEM permselectivity likely contributes to the CE losses observed for high-salinity feeds.

Conclusions

In this work we fabricated three pairs of high areal-loading electrodes (L: 15 mg cm^2, M: 19 mg cm^2, and H: 21 mg cm^2) that were embedded with interdigitated microchannels, and we desalinated water using them in a symmetric FDI flow cell with feed water recirculation. These electrodes are shown to reduce salt concentration from seawater salinity (496 mM NaCl) down to brackish water salinity (102 mM for L-pair), and to near freshwater salinity (23.7mM for M-pair and 19.1 mM for H-pair). The overall TEEs of these three experiments were 3.6%, 5.5%, and 7.4%, respectively, which are similar to past FDI studies that used brackish water feeds. H-pair electrodes were also used to treat hypersaline influent with 781 mM NaCl and were able to produce effluent of 227 mM at 11.7% TEE. This demonstrates for the first time the potential of symmetric FDI to treat concentrated brines. For brackish water influent of 118 mM NaCl, M- and H-pair electrodes comfortably produced effluents with freshwater salinities (16.7 mM and

512 7.8 mM) at TEEs of 40.0% and 23.6%, respectively. Moreover, these electrodes
513 exhibited outstanding cyclability with unnoticeable drops in specific capacity after 90
514 cycles. Despite this, mild yellowing of the AEM was observed after such experiments,
515 the effect of which we postulate as mild dehydrochlorination caused by weak Faradaic
516 side reactions at the electrode/AEM interface (see SI, Fig. S18). This study thus
517 demonstrates experimentally for the first time that FDI using scaled-up, high-capacity
518 electrodes can desalinate seawater-level salinity to near freshwater salinity, and it can
519 substantially decrease the salinity of hypersaline brines by resolving the issue of
520 pumping pressure/energy that is inherent to flow-through electrodes.

521 Factors contributing to energy efficiency losses are also identified. First, water
522 transport between diluate and brine was observed as high as 0.15 L m^{-2} h^{-1}, but water
523 recovery exceeding 50% was still obtained by using excess water initially in the diluate
524 reservoir. Second, the charge efficiency in the first half-cycle of desalination
525 experiments decreased from 91.7% to around 50% when feed concentration was varied
526 from 38 mM to greater than 500 mM. Chemical, physical, and electrochemical
527 interactions between porous electrode material, membrane material, and feed/effluent
528 solution therefore require further investigation to increase process efficiency, water
529 recovery, and water productivity.

530 We have demonstrated that minimizing the longitudinal hydraulic resistance within
531 microchannels relative to the transverse hydraulic resistance through intervening
532 porous-electrode material is critical to the effective use of eμ-IDFFs, thus demonstrating
533 the importance of flow-field co-design with the porous electrodes in which they are
534 embedded. Because electrode permeability scales with the square of particle size, eμ-

IDFFs are therefore likely to have broad impact on flow-through electrodes that incorporate fine-scale particles. Therefore, eμ-IDFFs could also find use in flow batteries, fuel cells, and CO_2 conversion electrodes that have employed nanomaterial catalysts[91–94] or conductive additives,[92] in addition to selective electrochemical removal and recovery processes. Water imbibition can also be used to protect other porous electrode materials during laser micromachining for Li-ion batteries[95] and micro-supercapacitors.[96]

Experimental Methods

Synthesis of NiHCF Nanoparticles

Nickel hexacyanoferrate (NiHCF) nanoparticles – a type of Prussian Blue analogue intercalation material – were prepared as in our previous work.[26] Two solutions of 0.1 M $K_3Fe(CN)_6$ and 0.2 M $NiCl_2$ with 1:1 volume ratio were added dropwise into a beaker containing deionized (DI) water and stirred vigorously at room temperature to obtain a suspension of NiHCF nanoparticles, which was then sonicated for 30 mins and aged overnight. The nanoparticles were subsequently collected by centrifugation and were rinsed with DI water and ethanol, followed by drying under vacuum at 80^{o}C.

Electrode Fabrication

Porous electrodes were made from 80:5:15 wt.% of NiHCF, Ketjen black (KB) conductive additive (EC-600JB), and polyvinylidene fluoride (PVDF) binder (Solvay Solef 5130), respectively. The mixture of NiHCF particles with KB was dry ground in a vortex mill using 5 mm steel balls (Ultra Turra-X, IKA) at 6000 rpm for 30 minutes to

558 obtain a fine, homogeneous powder. PVDF was dissolved in N-methyl-2-pyrrolidone
559 (NMP, Sigma Aldrich) to obtain a viscous, transparent liquid. The NiHCF and KB
560 powder mixture was added to this solution resulting in 3 mL of NMP per 1 g of solid
561 material. These components were homogenized in a planetary mixer (Thinky, ARE-
562 310) for 30 minutes. The resulting slurry was cast at thicknesses of 1.1 mm for L-pair
563 electrodes, 1.3 mm for M-pair electrodes, and 1.4 mm for H-pair electrodes onto
564 graphite-foil (Ceramaterials) current-collectors by using a doctor blade and film
565 applicator (Elcometer 4340). We note here that we typically use 1 g of solid materials for
566 one batch of slurry, and 1.4mm thick is the maximum thickness we could get to produce
567 a nice 4.5×4.5cm electrode after removing the material near the edges, which is prone
568 to crack during calendaring. Increasing the cast thickness further may cause the
569 electrode area to be smaller than 4.5×4.5cm with the prepared slurry. While making
570 more slurry by using more solid materials and NMP is feasible, we did not do that since
571 optimizing electrode mass loading is not the main focus of this study. Immediately after
572 casting, electrodes were immersed in an alkaline bath with pH=12 at 85^{o}C for
573 approximately 1 minute. These electrodes were then rinsed with DI water and
574 subsequently dried in a fume hood to produce thickness of greater than 400 μm. They
575 were then calendered down to ~200 μm using a roll press (MTI-XTL) and were
576 subsequently engraved with an interdigitated pattern over a 45 × 45 mm area. This
577 engraved area was then cut with scissors to obtain final electrodes.

578 *Porosity and Permeability Determination for Electrodes*

579 The porosity of each electrode ε was calculated from the electrode's measured
580 density ρ_e and the mass-averaged density ρ_c of its constituents (2.0 g cc^{-1} for NiHCF,[33]

2.0 g cc^{-1} for Ketjen Black,[97] and 1.75 g cc^{-1} for PVDF binder[98]) as $\varepsilon = 1 - \rho_e/\rho_c$. The permeability of each electrode with thickness t_e was measured using a gravity-driven apparatus[28] wherein a constant pressure head Δp (in units of Pa) was applied via a column of water to the FDI cell containing the targeted electrode. The amount of water permeating through the electrode over a certain period of time was used to calculate the average volumetric flow rate Q in units of m^3 s^{-1}. The permeability k_h in units of m^2 was then calculated from Darcy's law: $Q = \Delta p k_h W t_e / L\mu$, where μ is water's dynamic viscosity in Pa-s, and W and L are sample width and length, respectively.

Electrode Engraving by Laser Micromachining and Channel Characterization

eμ-IDFFs were engraved using a Trotec Speedy Flexx 400 laser. Immediately prior to water-imbibed engraving, dry electrodes were first soaked in DI water and subsequently wiped a Kimwipe to remove excess water. In all instances electrode engraving was conducted using ventilation to avoid human exposure to laser ablation products (e.g., HCN and HF). Optical profilometry (Keyence VK-X1000), Raman spectroscopy (Nanophoton Raman 11), and thermogravimetric analysis were used to characterize the composition and thermal stability of electrode materials in heat affected zones.

Symmetric FDI Cell Setup and Fluid Recirculation System

After laser engraving, electrodes with 45 × 45 mm size were cycled at a C-rate of C/10 in a three-electrode setup in 500 mM NaCl with an Ag/AgCl reference electrode (0.197 V vs. SHE) and a potentiostat (Biologic VMP-3). This step was used to remove Na^+ and K^+ present in the NiHCF crystal lattice during synthesis. Before being assembled in the FDI cell, one electrode was reduced to ~0% state-of-charge (SOC)

(0.1 V vs. Ag/AgCl) and the other one was oxidized to ~100% SOC (0.6 V vs. Ag/AgCl) by chronopotentiometry in a three-electrodes set up.

The FDI cell used in this study (Fig. 4a) is a scaled-up version of the cell used in our previous work[26] that contains two 45 × 45 mm electrodes separated by an anion-exchange membrane (Neosepta AMX). In all experiments a potentiostat (Biologic VMP-3) was used to control electrochemical cycling. A four-probe connection scheme (i.e., a Kelvin sensing measurement) was used to mitigate contact resistance between the potentiostat and the flow cell, as illustrated by distinct leads for sensing voltage and driving current in Fig. 4a. Salt concentrations used to calculate salt removal were determined by ion chromatography performed using a 930 Compact IC system from Metrohm with a Metrosep C4 – 150/4.0 cation column. Real-time conductivity of the reservoirs was collected using the Conduino system.[99]

Performance metrics

Thermodynamic energy efficiency:

TEE for a desalination experiment was calculated as:

$$TEE = \frac{SEC_{min}}{SEC} \times 100$$

The specific energy consumption SEC (kJ mol^{-1}) was calculated by dividing the total electrical energy input to the moles of salt removed from diluate stream into brine stream n_{salt}, which was measured at the end of the experiment:

$$SEC = \frac{\int_{t_0}^{t_{end}} I(t)V(t)dt}{n_{salt}}$$

with $I(t)$ and $V(t)$ respectively being the applied current and full-cell potential at time t. The minimum specific energy consumption was calculated per mole of salt removed as:

626 $$SEC_{min} = \frac{W_{rev}}{n_{salt}}$$

627 Here, the reversible work of separation W_{rev} was calculated using non-ideal activity
628 coefficients due to the high-salinity feeds used in our experiments and the hypersaline
629 brines produced from them:

630 $$W_{rev} = 2RT\left[V_D C_D \ln\left(f_{\pm}^{C_D} C_D\right) + V_B C_B \ln\left(f_{\pm}^{C_B} C_B\right) - (V_D + V_B) C_F \ln\left(f_{\pm}^{C_F} C_F\right)\right]$$

631 Here, V_i and C_i are respectively the volume of water and salt concentration of solution i,
632 where $i = B$, D, and F respectively refer to brine, diluate, and feed. The mean activity
633 coefficient $f_{\pm}^{C}$ was estimated for a given salt concentration C using literature data.[100]

634 *Charge efficiency*

635 Charge efficiency was calculated from the ratio of the moles of electrons
636 transferred throughout an experiment n_{charge} to the moles of salt removed n_{salt}:

637 $$CE = \frac{n_{salt}}{n_{charge}} \times 100\%$$

638 *Water recovery*

639 Water recovery was calculated at the end of each desalination half-cycle by
640 using the volumes of the diluate V_D and brine V_B reservoirs, assuming that salt and
641 liquid volume were conserved:

642 $$WR = \frac{V_D}{V_D + V_B} \times 100\%$$

643 *Water transport*

644 The water transport in each experiment was calculated as the difference between
645 the volume of the diluate reservoir initially (V_D^0) and after the experiment finished (V_D^{end}),

divided by the time duration of the experiment Δt and the area of the anion exchange membrane A_{AEM}:

$$J_w = \frac{V_D^0 - V_D^{end}}{\Delta t A_{AEM}}$$

Simulation of Flow through Electrodes with eμ-IDFFs

Flow-through electrodes embedded with eμ-IDFFs were modeled using conservation of fluid volume with a Darcy-type rate law for superficial velocity $\vec{u}_s$, as described already ($\vec{u}_s = -(k_h/\mu)\nabla p$). For each (x, y) location inside of a microchannel region we used $k_h(x, y) = k_h^{ch}$, where k_h^{ch} was calculated based on the Boussinesq solution for Poiseuille flow through a channel of rectangular cross-section with h-by-l size (see SI):[101]

$$k_h^{ch} = \frac{h^2}{12} - \frac{16h^3}{l\pi^5}\sum_{n=1}^{\infty}\frac{1}{(2n-1)^5}\frac{\cosh(\beta_n l) - 1}{\sinh(\beta_n l)} \quad (3)$$

Otherwise $k_h(x, y) = k_h^{pe}$ was used. The numerical solution for $\vec{u}_s$, obtained via the finite volume method implemented in MATLAB and solved using an aggregation-based algebraic multigrid method,[102–104] was then used to calculate the stream function[105] ψ via numerical integration:

$$\psi(x, y) = \psi_0 + \int_{(x_0, y_0)}^{(x,y)} u_s(x)dy - u_s(y)dx \quad (4)$$

Equally spaced contours of ψ were then used to determine streamlines.

Acknowledgements

The Expeditionary Energy Program of the US Office of Naval Research (Award no. N00014-22-1-2577), the Chemical, Bioengineering, Environmental and Transport Systems Division of the US National Science Foundation (Award no. 1931659), and the Department of Mechanical Science and Engineering at the University of Illinois at Urbana-Champaign (UIUC) supported this research. Thermogravimetric analysis, optical profilometry, and Raman spectroscopy were performed at the Materials Research Laboratory at UIUC. We thank Neil Pearse and Michael Dalton for the use of the Trotec Speedy Flexx 400 Laser in the Siebel Center for Design at UIUC. We thank Paolo Luzzatto-Fegiz for sharing the Conduino system used here. We thank Rob Roberts, Patrick Fahey, and Yarik Syzdek of Biologic for helpful conversations about Kelvin sensing and conductivity measurement by impedance. We thank Nouryon Chemicals for providing Ketjen black material, and we thank All Foils for providing thin Al foil for laser testing.

Conflicts of Interest

KCS, VQD, ERR, and ICL declare their filing of a related patent application.

References

1. Ihsanullah, I., Atieh, M. A., Sajid, M. & Nazal, M. K. Desalination and environment: A critical analysis of impacts, mitigation strategies, and greener desalination technologies. *Sci. Total Environ.* **780,** 146585 (2021).
2. Jones, E., Qadir, M., van Vliet, M. T. H., Smakhtin, V. & Kang, S. mu. The state of

desalination and brine production: A global outlook. *Sci. Total Environ.* **657,** 1343–1356 (2019).

3. Panagopoulos, A. Water-energy nexus: desalination technologies and renewable energy sources. *Environ. Sci. Pollut. Res.* **28,** 21009–21022 (2021).

4. D.S. Sholl & Lively, R. P. Seven chemical separations to change the world. *Nature* **532,** 435–437 (2016).

5. Anderson, M. A., Cudero, A. L. & Palma, J. Capacitive deionization as an electrochemical means of saving energy and delivering clean water. Comparison to present desalination practices: Will it compete? *Electrochim. Acta* **55,** 3845–3856 (2010).

6. Subramani, A. & Jacangelo, J. G. Treatment technologies for reverse osmosis concentrate volume minimization: A review. *Sep. Purif. Technol.* **122,** 472–489 (2014).

7. El Azhar, F., Tahaikt, M., Zouhri, N., Zdeg, A., Hafsi, M., Tahri, K., Bari, H., Taky, M., Elamrani, M. & Elmidaoui, A. Remineralization of Reverse Osmosis (RO)-desalted water for a Moroccan desalination plant: Optimization and cost evaluation of the lime saturator post. *Desalination* **300,** 46–50 (2012).

8. Yermiyahu, U., Tal, A., Ben-Gal, A. & Bar-Tal, A. Rethinking Desalinated Water Quality and Agriculture. *Science (80-.).* **318,** 920–921 (2007).

9. Elimelech, M. & Phillip, W. A. The future of seawater desalination: energy, technology, and the environment. *Science (80-.).* **333,** 712–717 (2011).

10. McGovern, R. K., Zubair, S. M. & Lienhard V, J. H. Hybrid electrodialysis reverse osmosis system design and its optimization for treatment of highly saline brines.

IDA J. Desalin. Water Reuse **6,** 15–23 (2014).

11. Bitaw, T. N., Park, K., Kim, J., Chang, J. W. & Yang, D. R. Low-recovery, -energy-consumption, -emission hybrid systems of seawater desalination: Energy optimization and cost analysis. *Desalination* **468,** 114085 (2019).
12. Loganathan, K., Chelme-Ayala, P. & Gamal El-Din, M. Treatment of basal water using a hybrid electrodialysis reversal-reverse osmosis system combined with a low-temperature crystallizer for near-zero liquid discharge. *Desalination* **363,** 92–98 (2015).
13. Oren, Y., Korngold, E., Daltrophe, N., Messalem, R., Volkman, Y., Aronov, L., Weismann, M., Bouriakov, N., Glueckstern, P. & Gilron, J. Pilot studies on high recovery BWRO-EDR for near zero liquid discharge approach. *Desalination* **261,** 321–330 (2010).
14. Porada, S., Zhao, R., van der Wal, A., Presser, V. & Biesheuvel, P. M. Review on the science and technology of water desalination by capacitive deionization. *Prog. Mater. Sci.* **58,** 1388–1442 (2013).
15. Huang, Z. H., Yang, Z., Kang, F. & Inagaki, M. Carbon electrodes for capacitive deionization. *J. Mater. Chem. A* **5,** 470–496 (2017).
16. Liu, Y., Nie, C., Liu, X., Xu, X., Sun, Z. & Pan, L. Review on carbon-based composite materials for capacitive deionization. *RSC Adv.* **5,** 15205–15225 (2015).
17. Suresh, A., Hill, G. T., Hoenig, E. & Liu, C. Electrochemically mediated deionization: a review. *Mol. Syst. Des. Eng.* **6,** 25–51 (2021).
18. Patel, S. K., Ritt, C. L., Deshmukh, A., Wang, Z., Qin, M., Epsztein, R. &

736 Elimelech, M. The relative insignificance of advanced materials in enhancing the
737 energy efficiency of desalination technologies. *Energy Environ. Sci.* **13,** 1694–
738 1710 (2020).
739 19. Wang, L., Dykstra, J. E. & Lin, S. Energy Efficiency of Capacitive Deionization.
740 *Environ. Sci. Technol.* **53,** 3366–3378 (2019).
741 20. Suss, M. E., Porada, S., Sun, X., Biesheuvel, P. M., Yoon, J. & Presser, V. Water
742 desalination via capacitive deionization: what is it and what can we expect from it?
743 *Energy Environ. Sci.* **8,** 2296–2319 (2015).
744 21. Tang, W., Liang, J., He, D., Gong, J., Tang, L., Liu, Z., Wang, D. & Zeng, G.
745 Various cell architectures of capacitive deionization: Recent advances and future
746 trends. *Water Res.* **150,** 225–251 (2019).
747 22. Pasta, M., Wessells, C. D., Cui, Y. & La Mantia, F. A desalination battery. *Nano*
748 *Lett.* **12,** 839–843 (2012).
749 23. Lee, J., Kim, S. & Yoon, J. Rocking Chair Desalination Battery Based on Prussian
750 Blue Electrodes. *ACS Omega* **2,** 1653–1659 (2017).
751 24. Smith, K. C. & Dmello, R. D. Na-Ion Desalination (NID) Enabled by Na-Blocking
752 Membranes and Symmetric Na-Intercalation: Porous-Electrode Modeling. *J.*
753 *Electrochem. Soc.* **163,** A530–A539 (2016).
754 25. Smith, K. C. Theoretical evaluation of electrochemical cell architectures using
755 cation intercalation electrodes for desalination. *Electrochim. Acta* **230,** 333–341
756 (2017).
757 26. Reale, E. R., Regenwetter, L., Agrawal, A., Dardón, B., Dicola, N., Sanagala, S. &
758 Smith, K. C. Low porosity, high areal-capacity Prussian blue analogue electrodes

enhance salt removal and thermodynamic efficiency in symmetric Faradaic deionization with automated fluid control. *Water Res. X* **13,** 100116 (2021).

27. Cao, J., Wang, Y., Wang, L., Yu, F. & Ma, J. Na 3 V 2 (PO 4) 3 @C as Faradaic Electrodes in Capacitive Deionization for High-Performance Desalination. *Nano Lett.* **19,** 823–828 (2019).

28. Reale, E. R., Shrivastava, A. & Smith, K. C. Effect of conductive additives on the transport properties of porous flow-through electrodes with insulative particles and their optimization for Faradaic deionization. *Water Res.* **165,** 114995 (2019).

29. Pothanamkandathil, V., Fortunato, J. & Gorski, C. A. Electrochemical Desalination Using Intercalating Electrode Materials: A Comparison of Energy Demands. *Environ. Sci. Technol.* **54,** 3653–3662 (2020).

30. Son, M., Pothanamkandath, V., Yang, W., Vrouwenvelder, J., Gorski, C. A. & Logan, B. E. Improving the Thermodynamic Energy Efficiency of Battery Electrode Deionization Using Flow-Through Electrodes. *Environ. Sci. Technol.* (2020). doi:10.1021/acs.est.9b06843

31. Kim, T., Gorski, C. A. & Logan, B. E. Low Energy Desalination Using Battery Electrode Deionization. *Environ. Sci. Technol. Lett.* **4,** 444–449 (2017).

32. Ahn, J., Kim, S., Jeon, S. il, Lee, C., Lee, J. & Yoon, J. Nafion-coated Prussian blue electrodes to enhance the stability and efficiency of battery desalination system. *Desalination* 114778 (2020). doi:10.1016/j.desal.2020.114778

33. Porada, S., Shrivastava, A., Bukowska, P., Biesheuvel, P. M. & Smith, K. C. Nickel Hexacyanoferrate Electrodes for Continuous Cation Intercalation Desalination of Brackish Water. *Electrochim. Acta* **255,** 369–378 (2017).

34. Liu, Y., Wang, K., Xu, X., Eid, K., Abdullah, A. M., Pan, L. & Yamauchi, Y. Recent Advances in Faradic Electrochemical Deionization: System Architectures versus Electrode Materials. *ACS Nano* **15,** 13924–13942 (2021).

35. Smith, K. C. & Dmello, R. D. Desalination Devices. *US Pat. No.* 11,053,142 (2021).

36. Liu, S. & Smith, K. C. Quantifying the Trade-offs between Energy Consumption and Salt Removal Rate in Membrane-free Cation Intercalation Desalination. *Electrochim. Acta* **271,** 652–665 (2018).

37. Li, Q., Zheng, Y., Xiao, D., Or, T., Gao, R., Li, Z., Feng, M., Shui, L., Zhou, G., Wang, X. & Chen, Z. Faradaic Electrodes Open a New Era for Capacitive Deionization. *Adv. Sci.* **7,** (2020).

38. Suss, M. E., Baumann, T. F., Bourcier, W. L., Spadaccini, C. M., Rose, K. A., Santiago, J. G. & Stadermann, M. Capacitive desalination with flow-through electrodes. *Energy Environ. Sci.* **5,** 9511–9519 (2012).

39. Guyes, E. N., Simanovski, A. & Suss, M. E. Several orders of magnitude increase in the hydraulic permeability of flow-through capacitive deionization electrodes via laser perforations. *RSC Adv.* **7,** 21308–21313 (2017).

40. Bhattarai, A., Wai, N., Schweiss, R., Whitehead, A., Lim, T. M. & Hng, H. H. Advanced porous electrodes with flow channels for vanadium redox flow battery. *J. Power Sources* **341,** 83–90 (2017).

41. Dennison, C. R., Agar, E., Akuzum, B. & Kumbur, E. C. Enhancing Mass Transport in Redox Flow Batteries by Tailoring Flow Field and Electrode Design. *J. Electrochem. Soc.* **163,** A5163–A5169 (2016).

42. Sauermoser, M., Kizilova, N., Pollet, B. G. & Kjelstrup, S. Flow Field Patterns for Proton Exchange Membrane Fuel Cells. *Front. Energy Res.* **8,** 1–20 (2020).
43. Zeng, Y., Li, F., Lu, F., Zhou, X., Yuan, Y., Cao, X. & Xiang, B. A hierarchical interdigitated flow field design for scale-up of high-performance redox flow batteries. *Appl. Energy* **238,** 435–441 (2019).
44. Lu, M., Jiao, Y., Tang, X., Yang, W., Ye, M. & Xu, Q. Blocked serpentine flow field with enhanced species transport and improved flow distribution for vanadium redox flow battery. *J. Energy Storage* **35,** 102284 (2021).
45. Aparicio-Mauricio, G., Rodríguez, F. A., Pijpers, J. J. H., Cruz-Díaz, M. R. & Rivero, E. P. CFD modeling of residence time distribution and experimental validation in a redox flow battery using free and porous flow. *J. Energy Storage* **29,** 101337 (2020).
46. Gundlapalli, R., Bhattarai, A., Ranjan, R., Ghimire, P. C., Yeo, X. M., Bin Zainudin, N. A., Wai, N., Mahlendorf, F., Jasincuk, A. & Thorsten, H. Characterization and scale-up of serpentine and interdigitated flow fields for application in commercial vanadium redox flow batteries. *J. Power Sources* **542,** 231812 (2022).
47. Macdonald, M. & Darling, R. M. Comparing velocities and pressures in redox flow batteries with interdigitated and serpentine channels. *AIChE J.* **65,** 1–11 (2019).
48. Gundlapalli, R. & Jayanti, S. Effect of channel dimensions of serpentine flow fields on the performance of a vanadium redox flow battery. *J. Energy Storage* **23,** 148–158 (2019).
49. Gundlapalli, R. & Jayanti, S. Effect of electrolyte convection velocity in the

electrode on the performance of vanadium redox flow battery cells with serpentine flow fields. *J. Energy Storage* **30,** (2020).

50. Gundlapalli, R. & Jayanti, S. Effective splitting of serpentine flow field for applications in large-scale flow batteries. *J. Power Sources* **487,** 229409 (2021).

51. Pichugov, R. D., Konev, D. V., Petrov, M. M., Antipov, A. E., Loktionov, P. A., Abunaeva, L. Z., Usenko, A. A. & Vorotyntsev, M. A. Electrolyte Flow Field Variation: A Cell for Testing and Optimization of Membrane Electrode Assembly for Vanadium Redox Flow Batteries. *Chempluschem* **85,** 1919–1927 (2020).

52. Sun, J., Zheng, M., Yang, Z. & Yu, Z. Flow field design pathways from lab-scale toward large-scale flow batteries. *Energy* **173,** 637–646 (2019).

53. Wan, S., Jiang, H., Guo, Z., He, C., Liang, X., Djilali, N. & Zhao, T. Machine learning-assisted design of flow fields for redox flow batteries. *Energy Environ. Sci.* **15,** 2874–2888 (2022).

54. Tsushima, S. & Suzuki, T. Modeling and Simulation of Vanadium Redox Flow Battery with Interdigitated Flow Field for Optimizing Electrode Architecture. *J. Electrochem. Soc.* **167,** 020553 (2020).

55. MacDonald, M. & Darling, R. M. Modeling flow distribution and pressure drop in redox flow batteries. *AIChE J.* **64,** 3746–3755 (2018).

56. Xu, Z., Wang, J., Yan, S. C., Fan, Q. & Lund, P. D. Modeling of Zinc Bromine redox flow battery with application to channel design. *J. Power Sources* **450,** 227436 (2020).

57. Yadav, S. & Krishnamurthy, B. Modeling the velocity profiles in Vanadium Redox flow batteries-Serpentine flow field. *J. Electrochem. Sci. Eng.* **00,** 1–16 (2023).

58. Li, F., Wei, Y., Tan, P., Zeng, Y. & Yuan, Y. Numerical investigations of effects of the interdigitated channel spacing on overall performance of vanadium redox flow batteries. *J. Energy Storage* **32,** 101781 (2020).

59. Akuzum, B., Alparslan, Y. C., Robinson, N. C., Agar, E. & Kumbur, E. C. Obstructed flow field designs for improved performance in vanadium redox flow batteries. *J. Appl. Electrochem.* **49,** 551–561 (2019).

60. Gundlapalli, R. & Jayanti, S. Performance characteristics of several variants of interdigitated flow fields for flow battery applications. *J. Power Sources* **467,** 228225 (2020).

61. Zeng, Y. K., Zhou, X. L., Zeng, L., Yan, X. H. & Zhao, T. S. Performance enhancement of iron-chromium redox flow batteries by employing interdigitated flow fields. *J. Power Sources* **327,** 258–264 (2016).

62. Ke, X., Prahl, J. M., Alexander, J. I. D. & Savinell, R. F. Redox flow batteries with serpentine flow fields: Distributions of electrolyte flow reactant penetration into the porous carbon electrodes and effects on performance. *J. Power Sources* **384,** 295–302 (2018).

63. Eifert, L., Bevilacqua, N., Kçble, K., Fahy, K., Liusheng Xiao, Li, M., Duan, K., Bazylak, A., Sui, P.-C. & Zeis, R. Synchrotron X-ray Radiography and Tomography of Vanadium Redox Flow Batteries Cell Design, Electrolyte, Flow Geometry, and Gas Bubble Formation. *ChemSusChem* **13,** 3154–3165 (2020).

64. Darling, R. M. & Perry, M. L. The influence of electrode and channel configurations on flow battery performance. *J. Electrochem. Soc.* **161,** A1381--A1387 (2014).

65. Sun, J., Jiang, H. R., Zhang, B. W., Chao, C. Y. H. & Zhao, T. S. Towards uniform distributions of reactants via the aligned electrode design for vanadium redox flow batteries. *Appl. Energy* **259,** 114198 (2020).
66. Ha, J., Choi, Y. Y., Kim, Y., Lee, J. N. & Choi, J. Il. Two-layer hydrodynamic network model for redox flow battery stack with flow field design. *Int. J. Heat Mass Transf.* **201,** 123626 (2023).
67. Bhattarai, A., Wai, N., Schweiss, R., Whitehead, A., Scherer, G. G., Ghimire, P. C., Lim, T. M. & Hng, H. H. Vanadium redox flow battery with slotted porous electrodes and automatic rebalancing demonstrated on a 1 kW system level. *Appl. Energy* **236,** 437–443 (2019).
68. Tu, Y. H., Tai, Y. C., Xu, J. Y., Yang, Y. H., Huang, H. Y., Huang, J. H. & Hu, C. C. Highly efficient water purification devices utilizing the microfluidic electrochemical deionization technique. *Desalination* **538,** 115928 (2022).
69. Lisboa, K. M., Marschewski, J., Ebejer, N., Ruch, P., Cotta, R. M., Michel, B. & Poulikakos, D. Mass transport enhancement in redox flow batteries with corrugated fluidic networks. *J. Power Sources* **359,** 322–331 (2017).
70. Ke, X., Prahl, J. M., Alexander, I. J. D., Wainright, J. S., Zawodzinski, T. A. & Savinell, R. F. Rechargeable redox flow batteries: Flow fields, stacks and design considerations. *Chem. Soc. Rev.* **47,** 8721–8743 (2018).
71. Gundlapalli, R. & Jayanti, S. Effect of electrode compression and operating parameters on the performance of large vanadium redox flow battery cells. *J. Power Sources* **427,** 231–242 (2019).
72. Charvát, J., Mazúr, P., Dundálek, J., Pocedič, J., Vrána, J., Mrlík, J., Kosek, J. &

Dinter, S. Performance enhancement of vanadium redox flow battery by optimized electrode compression and operational conditions. *J. Energy Storage* **30,** (2020).

73. Witherspoon, P. A., Wang, J. S. Y., Iwai, K. & Gale, J. E. Validity of Cubic Law for Fluid Flow in a Deformable Rock Fracture. **16,** 1016–1024 (1980).

74. Inoue, M., Tada, Y., Suganuma, K. & Ishiguro, H. Thermal stability of poly(vinylidene fluoride) films pre-annealed at various temperatures. *Polym. Degrad. Stab.* **92,** 1833–1840 (2007).

75. Li, J. & Ananthasuresh, G. K. A quality study on the excimer laser micromachining of electro-thermal-compliant micro devices. *ASME Int. Mech. Eng. Congr. Expo. Proc.* **2000-AB,** 687–694 (2000).

76. Kruusing, A., Leppävuori, S., Uusimäki, A., Petrêtis, B. & Makarova, O. Micromachining of magnetic materials. *Sensors Actuators, A Phys.* **74,** 45–51 (1999).

77. Bergman, T. & Lavine, A. *Fundamentals of Heat and Mass Transfer*. (Wiley, 2017).

78. Park, H. K., Zhang, X., Grigoropoulos, C. P., Poon, C. C. & Tam, A. C. Transient temperature during the vaporization of liquid on a pulsed laser-heated solid surface. *J. Heat Transfer* **118,** 702–708 (1996).

79. Lin, S. Energy Efficiency of Desalination: Fundamental Insights from Intuitive Interpretation. *Environ. Sci. Technol.* **54,** 76–84 (2020).

80. Liu, H. & She, Q. Influence of membrane structure-dependent water transport on conductivity-permselectivity trade-off and salt/water selectivity in electrodialysis: Implications for osmotic electrodialysis using porous ion exchange membranes. *J.*

Memb. Sci. **650,** 120398 (2022).

81. Tedesco, M., Hamelers, H. V. M. V. M. & Biesheuvel, P. M. M. Nernst-Planck transport theory for (reverse) electrodialysis: II. Effect of water transport through ion-exchange membranes. *J. Memb. Sci.* **531,** 172–182 (2017).

82. Jiang, C., Wang, Q., Li, Y., Wang, Y. & Xu, T. Water electro-transport with hydrated cations in electrodialysis. *Desalination* **365,** 204–212 (2015).

83. Kingsbury, R. S., Zhu, S., Flotron, S. & Coronell, O. Microstructure Determines Water and Salt Permeation in Commercial Ion-Exchange Membranes. *ACS Appl. Mater. Interfaces* **10,** 39745–39756 (2018).

84. Yan, H., Wang, Y., Wu, L., Shehzad, M. A., Jiang, C., Fu, R., Liu, Z. & Xu, T. Multistage-batch electrodialysis to concentrate high-salinity solutions: Process optimisation, water transport, and energy consumption. *J. Memb. Sci.* **570–571,** 245–257 (2019).

85. Darling, R. M., Weber, A. Z., Tucker, M. C. & Perry, M. L. The influence of electric field on crossover in redox-flow batteries. *J. Electrochem. Soc.* **163,** A5014–A5022 (2016).

86. Zhao, R., Biesheuvel, P. M., Miedema, H., Bruning, H. & van der Wal, A. Charge efficiency: A functional tool to probe the double-layer structure inside of porous electrodes and application in the modeling of capacitive deionization. *J. Phys. Chem. Lett.* **1,** 205–210 (2010).

87. Johnson, A. M. & Newman, J. Desalting by Means of Porous Carbon Electrodes. *J. Electrochem. Soc.* **118,** 510–517 (1971).

88. Hawks, S. A., Knipe, J. M., Campbell, P. G., Loeb, C. K., Hubert, M. A., Santiago,

J. G. & Stadermann, M. Quantifying the flow efficiency in constant-current capacitive deionization. *Water Res.* **129,** 327–336 (2018).

89. Yoon, J., Flavin, M. T. & Han, J. Current efficiency and selectivity reduction caused by co-ion leakage in electromembrane processes. *Water Res.* **201,** 117351 (2021).

90. Abu-Rjal, R., Chinaryan, V., Bazant, M. Z., Rubinstein, I. & Zaltzman, B. Effect of concentration polarization on permselectivity. *Phys. Rev. E - Stat. Nonlinear, Soft Matter Phys.* **89,** 1–10 (2014).

91. Lv, Y., Han, C., Zhu, Y., Zhang, T., Yao, S., He, Z., Dai, L. & Wang, L. Recent advances in metals and metal oxides as catalysts for vanadium redox flow battery: Properties, structures, and perspectives. *J. Mater. Sci. Technol.* **75,** 96–109 (2021).

92. Long, Y., Ding, M. & Jia, C. Application of Nanomaterials in Aqueous Redox Flow Batteries. *ChemNanoMat* **7,** 699–712 (2021).

93. Raduwan, N. F., Shaari, N., Kamarudin, S. K., Masdar, M. S. & Yunus, R. M. An overview of nanomaterials in fuel cells: Synthesis method and application. *Int. J. Hydrogen Energy* **47,** 18468–18495 (2022).

94. Yin, Z., Yu, C., Zhao, Z., Guo, X., Shen, M., Li, N., Muzzio, M., Li, J., Liu, H., Lin, H., Yin, J., Lu, G., Su, D. & Sun, S. Cu3n nanocubes for selective electrochemical reduction of co2 to ethylene. *Nano Lett.* 8658–8663 (2019). doi:10.1021/acs.nanolett.9b03324

95. Chen, K.-H., Namkoong, M. J., Goel, V., Yang, C., Kazemiabnavi, S., Mortuza, S. M., Kazyak, E., Mazumder, J., Thornton, K., Sakamoto, J. & Dasgupta, N. P.

Efficient fast-charging of lithium-ion batteries enabled by laser-patterned three-dimensional graphite anode architectures. *J. Power Sources* **471,** 228475 (2020).

96. Cao, L., Yang, S., Gao, W., Liu, Z., Gong, Y., Ma, L., Shi, G., Lei, S., Zhang, Y., Zhang, S., Vajtai, R. & Ajayan, P. M. Direct Laser-Patterned Micro-Supercapacitors from Paintable MoS 2 Films. *Small* **9,** 2905–2910 (2013).

97. Rossman, R. P. & Smith, W. R. Density of Carbon Black By Helium Displacement. *Ind. Eng. Chem.* **35,** 972–976 (1943).

98. Solvay. *Solef® PVDF Design & Processing Guide*. (2015).

99. Carminati, M. & Luzzatto-Fegiz, P. Conduino: Affordable and high-resolution multichannel water conductivity sensor using micro USB connectors. *Sensors Actuators, B Chem.* **251,** 1034–1041 (2017).

100. Hamer, W. J. & Yung chi, Y. Osmotic Coefficients and Mean Activity Coefficients of Uni univalent Electrolytes in Water at 25°C. *J. Phys. Chem. Ref. Data* **1,** 1047–1100 (1972).

101. Boussinesq, M. J. Mémoire sur l'influence des frottements dans les mouvements réguliers des fluides. *J. Math. Pure Appl.* **13,** 377–424 (1868).

102. Napov, A. & Notay, Y. An algebraic multigrid method with guaranteed convergence rate. *SIAM J. Sci. Comput.* **34,** A1079–A1109 (2012).

103. Notay, Y. An aggregation-based algebraic multigrid method. *Electron. Trans. Numer. Anal.* **37,** 123–146 (2010).

104. Notay, Y. Aggregation-based algebraic multigrid for convection-diffusion equations. *SIAM J. Sci. Comput.* **34,** A2288–A2316 (2012).

105. Batchelor, G. K. *An introduction to fluid dynamics*. (Cambridge University Press,

989 2000).

990